Influence of post-synthesis processing on the structure, transport, and performance of the solid electrolyte $Li_{5.5}PS_{4.5}Cl_{1.5}$ in all-solid-state batteries

Oliver Maus[a,b], Martin A. Lange[a], Finn Frankenberg[c], Florian Stainer[d], Vasiliki Faka[a], Eva Schlautmann[a], Carolin Rosenbach[a], Anna Jodlbauer[d], Johannes Schubert[e,f], Jürgen Janek[e,f], Cheng Li[g], Peter Michalowski[c], Martin Wilkening[d], Arno Kwade[c], Wolfgang G. Zeier[a,b,h]*

[a]*Institute of Inorganic and Analytical Chemistry, University of Münster, D-48149 Münster, Germany*

[b]*International Graduate School for Battery Chemistry, Characterization, Analysis, Recycling and Application (BACCARA), University of Münster, D-48149 Münster, Germany*

[c]*Technische Universität Braunschweig, Institute for Particle Technology, Volkmaroder Straße 5, D-38104 Braunschweig, Germany*

[d]*Institute of Chemistry and Technology of Materials, Graz University of Technology (NAWI Graz), Stremayrgasse 9, A-8010 Graz, Austria*

[e]*Institute of Physical Chemistry, Justus Liebig University, Heinrich-Buff-Ring 17, D-35392 Giessen, Germany*

[f]*Center for Materials Research (ZfM), Justus Liebig University, Heinrich-Buff-Ring 16, Giessen D-35392, Germany*

[g]*Neutron Science Division, Oak Ridge National Laboratory, Oak Ridge, TN 37830, USA*

[h]*Institut für Energie- und Klimaforschung (IEK), IEK-12: Helmholtz-Institut Münster, Forschungszentrum Jülich, D-48149 Münster, Germany*

Corresponding author email: wzeier@uni-muenster.de

Abstract

While post-synthesis processing steps are frequently applied in the preparation of cathode composites for solid-state batteries to ensure homogeneous mixing and good contact with the cathode active material, little is known about the processes that occur during milling and how they influence structure and transport of solid electrolytes. Here, we use an extensive set of experimental methods and simulations to study the effects of post-synthesis milling by a frequency and planetary ball mill on the highly conducting chloride-rich argyrodite $Li_{5.5}PS_{4.5}Cl_{1.5}$. Structural analyses show that processing can reduce the coherence length and increase the disorder. The reduced crystallite size correlates with a decrease in ionic conductivity in the post-processed solid electrolytes. Simulating the ball milling processes by the discrete element method provides fundamental understanding and reveals the correlation of the loss in coherence with the specific energy input and the numbers of stressing events during the milling process. An observed decrease in particle size in ball milled samples leads to lower tortuosity in the cathode composites. As the loss in coherence and decrease in particle size have opposite effects on the performance, optimizing these processing conditions will play a significant role on the road to highly performing solid-state batteries.

1. Introduction

The ongoing decarbonization and electrification of the mobility sector and other industrial sectors increases the demand in highly performing energy storage systems. All-solid-state batteries have the potential to achieve higher energy densities than conventional liquid lithium ion batteries[1] by enabling the use of lithium metal[2,3]or silicon alloys[4,5] as negative electrode. To achieve sufficient power densities, solid-state batteries require optimized solid electrolytes with an ionic conductivity above 10 mS/cm.[6] Over the last years, promising Li^+ ionic conductors in the classes of oxides, e.g. $Li_7La_3Zr_2O_{12}$,[7–9] halides, e.g Li_3MCl_6 (M^{3+} = e.g. Y, Er, In),[10,11] and thiophosphates, e.g. $Li_{10}GeP_2S_{12}$,[12,13] have been studied. The thiophosphate-based lithium argyrodite with a chemical formula of Li_6PS_5X (X = Cl, Br, I) has gained particular interest for applications due to its high ionic conductivity and relatively simple preparation.[14]

The argyrodite structure type (**Figure 1**a) exhibits $F\bar{4}3m$ space group symmetry in which the halide ions are located on a face-centered cubic sublattice (Wyckoff 4*a* position).[15] The PS_4^{3-} polyanions are filling the octahedral voids (P on Wyckoff 4*b*, S on 16*e*) while half of the tetrahedral voids are occupied by S^{2-} ions (Wyckoff 4*d*). Lithium ions (Wyckoff 48h) are forming partially occupied cages around the 4*d* position which allows rapid Li^+ diffusion.[16] In Li_6PS_5Cl, a site disorder between S^{2-} and Cl^- on the 4*d* and 4*a* is observed due to the similar ionic radii.[17,18] It is reported that the lower charge of Cl^- on the 4*d* position facilitates the interconnection of the Li^+ cages and thereby increase the Li^+ ionic conductivity.[19] The effect can be enhanced by substituting S^{2-} by Cl^- in $Li_{5.5}PS_{4.5}Cl_{1.5}$ to achieve an ionic conductivity of 7 - 8 mS/cm.[20] This high conductivity makes $Li_{5.5}PS_{4.5}Cl_{1.5}$ one of the most promising materials for high performing solid-state batteries.

A sufficiently high ionic conductivity is in particular needed in electrode composites (Figure 1b) where a good conduction and contact with the active material is crucial to access full capacities.[21] To reproducibly prepare homogeneous composites and ensure best connectivity, a mixing step is usually applied. Common processing methods include the use of a frequency ball mill (see schematic in Figure 1c) as applied in various publications with $LiNi_xCo_yMn_{1-x-y}O_2$ (NCM)[22,23] as cathode active material, while planetary ball mills are frequently used for lithium-sulfur solid-state batteries[24,25] as well as NCM-sulfide composites.[26]

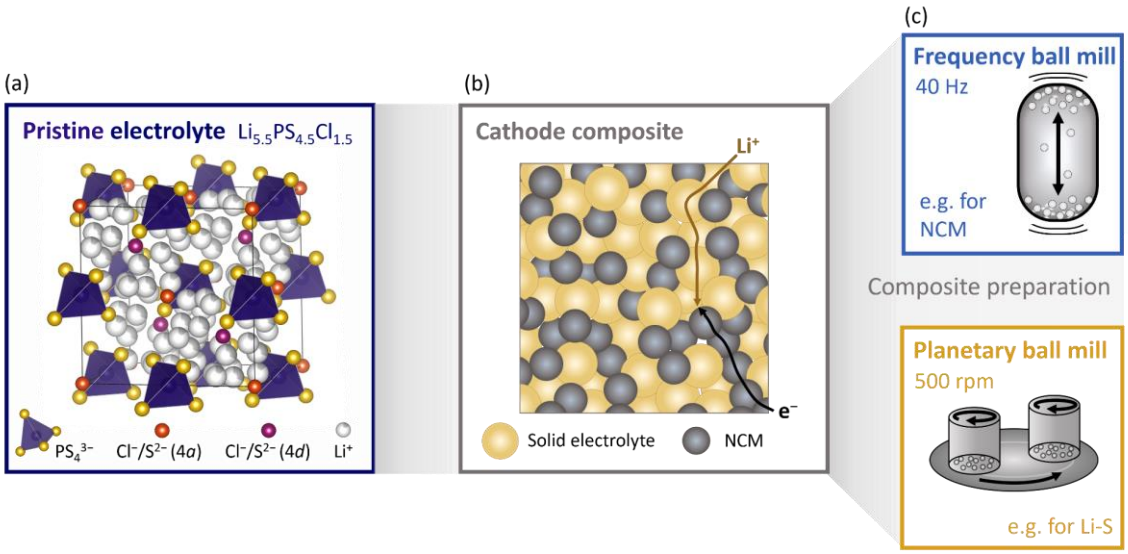


Figure 1: *(a) Crystal structure of the pristine $Li_{5.5}PS_{4.5}Cl_{1.5}$. (b) Cathode composite of solid electrolyte and cathode active material needs to ensure sufficient ionic and electronic transport. (c) Schematic representation of the working principles of the frequency ball mill and the planetary ball mill which are one of the main methods of processing for solid-state battery building.*

While post-synthesis processing steps are applied very frequently in the preparation of solid-state batteries, little is known about how exactly the processing step does influence the properties of the solid electrolyte. Recently, Schweiger *et al.* showed the effects of ball milling on $Li_{10}GeP_2S_{12}$ by nuclear magnetic resonance spectroscopy and found out that harsh ball milling leads to rapid amorphization with decreasing transport performance of the electrolyte.[27] Peng *et al.* used ball milling to obtain smaller particles of $Li_{5.5}PS_{4.5}Cl_{1.5}$ and thereby showed a decrease in the ionic conductivity.[28] Furthermore, changes in the microstructure of Li_6PS_5Cl due to wet milling affect the electrochemical stability against the lithium metal electrode.[29] Dewald *et al.* reported indications of lower coherence during the preparation of lithium-sulfur battery composites by ball milling.[30] In other cases where ball milling was used to synthesize solid-state electrolytes, clear changes of the local structure are observed.[31] While these results demonstrate that post-synthesis processing is decisive for the final properties of the solid electrolyte, questions about the actual processes occurring during milling remain open: What are the stresses acting on the solid electrolyte during milling? How do they affect the local structure, the crystallinity and the transport properties of the solid electrolyte? And what influence do the different processing parameters such as the processing method, the milling frequency, the milling time and the grinding media size have on the properties of the electrolyte and final cathode composite?

Inspired by the questions raised by these observations, we performed a systematic study on the effects of post-synthesis processing on the structure and transport properties of $Li_{5.5}PS_{4.5}Cl_{1.5.}$ Investigating the crystallinity and local structure by X-ray diffraction (XRD), X-ray pair distribution function (XPDF) and neutron pair distribution function (NPDF) analyses as well as nuclear magnetic resonance (NMR) spectroscopy, shows that ball milling clearly decreases the crystallite size while increased disorder in the local structure can be observed. Scanning electron microscopy and laser diffraction reveal smaller particle sizes in processed samples compared to pristine ones. These changes are partly reversible as annealed samples show. By performing discrete element simulations, differences in the specific energy input are revealed as major factor for the observed changes of the electrolyte for the first time. While the decrease in crystallinity with increasing energy input leads to reduced ionic conductivities, the smaller particles lead to lower tortuosity in cathode composites and better performance in solid state batteries. Due to these two opposite trends, short times of ball milling leads to the best capacities in solid-state battery half-cells. This work shows how important the influence of post processing composites is on the solid-state battery performance, an often-overlooked aspect in the research for improvement of solid electrolytes and solid-state batteries.

2. Results and Discussion

Effects on crystallinity and local structure. In order to investigate the effect of different processing methods on the solid electrolytes, one large batch of $Li_{5.5}PS_{4.5}Cl_{1.5}$ was prepared via a modified route of a previously reported solid-state synthesis.[20] Rietveld refinement confirms the successful synthesis of the nearly phase pure solid electrolyte, only a minor LiCl phase fraction around 1 wt.% can be found (Figure S1). This batch was split into groups which were processed at three different conditions resembling the typical conditions of solid-state battery preparation. One part was treated in a frequency ball mill at 40 Hz for 10 min and another part was processed in a planetary ball mill for 240 min to resemble the standard conditions for the preparation of lithium sulfur solid state batteries.[32] A third part was processed at 500 rpm for 10 min to compare both methods. For all methods grinding media with a size of 5 mm was used. To study the effect of the processing on the crystal structure of the material, X-ray diffraction was carried out. For all samples, the diffraction pattern (Figure S2) and diffraction peak position did not change significantly showing that the overall symmetry and crystal structure is retained. However, for the samples processed in the planetary ball mill diffraction peak broadening can be observed, most pronounced after four hours of processing (**Figure 2**a). This broadening

indicates lower crystallinity and the presence of internal strain. Simultaneously, the increase of a broad background with the ball milling shows increased diffuse scattering and potentially lower coherence.

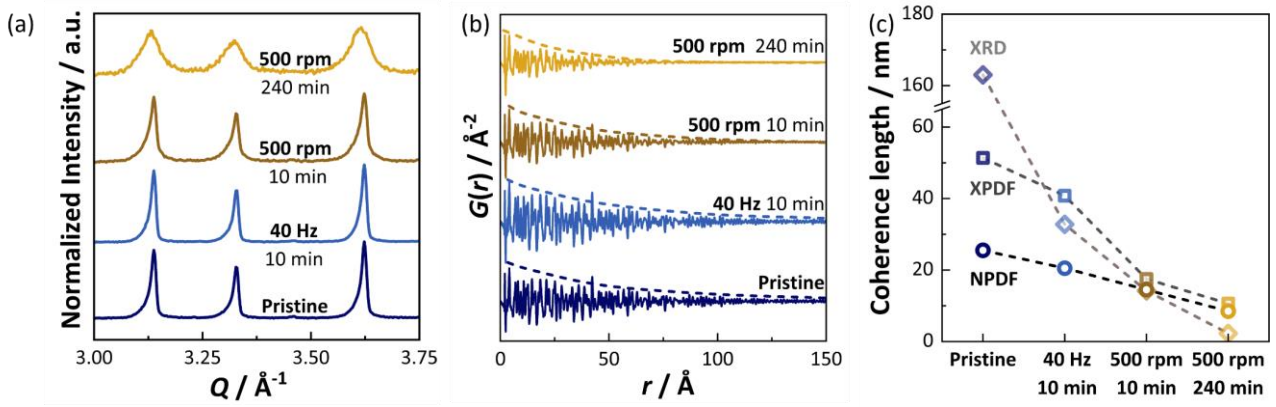


Figure 2: *(a) X-ray diffractogram of $Li_{5.5}PS_{4.5}Cl_{1.5}$ processed with 5 mm grinding media at different processing conditions demonstrates the broadening of the reflections with increasing ball milling time. (b) The long-range neutron pair distribution function data shows faster decay of G(r) for the ball milled samples which was fit to extract coherence lengths. (c) Extracted coherence lengths by small box modelling of NPDF and XPDF data and crystallite size from Rietveld refinement of the X-ray diffraction data.*

In addition to X-ray diffraction, complementary NPDF and XPDF analyses were performed to study the local structure of the materials. For a PDF analysis, the total scattering of the sample is measured over a large *Q*-range and a histogram of atom-atom distances is obtained via Fourier transformation. The large *r*-range of the NPDF of the differently processed samples (Figure 2b) reveals differences in the coherence length. While the NPDF of the pristine sample and the one processed in the frequency ball mill at 40 Hz still show clear signals above 100 Å, the samples milled at 500 rpm exhibit a faster decay in intensity. A similar decay for the samples processed at 500 rpm can be observed in the XPDF data (Figure S3). Small box modelling with a spherical domain model allows to fit the decay of neutron and X-ray PDF by an envelope function and gives a quantitative estimation of the coherence length, i.e. the mean size of crystalline domains.[33] For the Bragg diffraction data, Rietveld refinement is used to extract the crystallite size and strain contribution of the peak broadening.[34] The induced strain is further analyzed by the Williamson-Hall method[35] on X-ray Bragg data measured on a copper diffractometer. The coherence lengths extracted by the described methods from NPDF and XPDF as well as Rietveld refinement are displayed in Figure 2c. All methods show the same relative reduction in the coherence length of $Li_{5.5}PS_{4.5}Cl_{1.5}$ with processing, especially when using the planetary ball mill. The extracted absolute values differ mostly for the pristine sample. With higher

crystallite sizes the inaccuracy of the methods drastically increases leading to this spread for the pristine sample.[36] In addition to the decrease in crystallinity, the Williamson-Hall analyses also show an increase in internal strain for the samples that were processed in the planetary ball mill (Figure S4). The strain values obtained by Rietveld refinement exhibit the same trend as the Williamson-Hall analyses and only differ in the proportionality factor (Figure S5).

While the decay in intensity at higher atom – atom distances shows the difference in coherence length, the low *r* region of the NPDF (**Figure 3**a) gives information about the local structure. The positive peak at 2.04 Å corresponds to the P-S bond in the PS_4^{3-} unit, while the one at 2.44 Å corresponds to the closest Li^+-Cl^-/S^{2-}(4*d*) and is negative due to the negative neutron scattering length of ^{7}Li. These first peaks do not change for the differently processed samples showing that the rigid PS_4^{3-} polyanion and the first coordination sphere is not affected by ball milling. However, peaks at higher *r* broaden for the samples processed at 500 rpm with a lower maximum intensity indicating increased disorder in higher coordination spheres. The increased disorder correlates with the loss in crystallinity and reduced coherence length. Comparison of the NPDF transformed at different Q_{max} values confirms that the observed broadening is not caused by transformation artefacts but can be assigned to structural changes (Figure S6). Small-box modelling of the pristine NPDF (Figure S7a) by the cubic structural model results in a deviation between observed and calculated *G*(*r*) around 4 Å. Schlenker *et al.* observed for the X-ray PDF of Li_6PS_5Cl discrepancies from the cubic structural model between 3 Å and 4.5 Å which could be fitted by a tilting of the PS_4^{3-} polyanions in a monoclinic model.[37] Based on the cubic model of $Li_{5.5}PS_{4.5}Cl_{1.5}$ a similar monoclinic model with *Cm* symmetry and rotationally disordered PS_4^{3-} polyanions was used to fit the neutron PDF data (Figure S8a and b). For the pristine sample, this model (Figure S8c) results in slightly better fit residuals and in a lower atomic displacement parameter for the PS_4^{3-} polyanion (Table S6). As this result may indicate the presence of tilted polyanions in the local structure of pristine $Li_{5.5}PS_{4.5}Cl_{1.5,}$ it leads to the hypothesis that an increase in rotational disorder of PS_4^{3-} polyanions is one of the reasons for the broadened peaks at 500 rpm. However, refining only the rotational disorder in the small box model did not fit the broadening of signals in the ball milled sample. The PDF of the samples processed at 500 rpm could only be fitted with high atomic displacement parameters for all atoms, demonstrating the induced disorder in the local structure. Similar broadening in the XPDF (Figure S9) is observed which further shows increased disorder in the local structure for samples processed in the planetary ball mill.

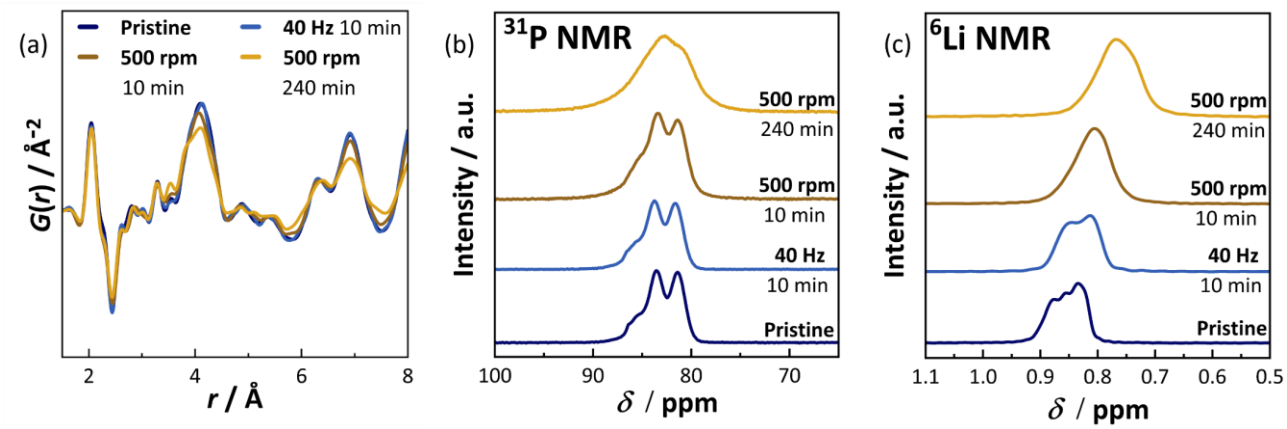


Figure 3: *(a) Broadening of peaks and lower maximum intensity above 4 Å in the NPDF of samples milled at 500 rpm reveals increased disorder in the local structure. (b)* ^{31}*P MAS NMR and (c)* ^{6}*Li MAS NMR spectra of pristine and processed* $Li_{5.5}PS_{4.5}Cl_{1.5}$ *show broadened resonances for the sample milled for four hours.*

^{31}P and ^{6}Li magic angle spinning (MAS) NMR measurements help to gain further information about the disorder in the local structure observed in PDF. Due to the Cl^{-}/S^{2-} disorder on the Wyckoff 4*d* position, each PS_4^{3-} polyanion can have five different combinations of ions on the four nearest Wyckoff 4*d* positions as reported for the structurally similar Li_6PS_5Br.[38] These different coordination possibilities lead to the line splitting observed in ^{31}P NMR (Figure 3b) of pristine $Li_{5.5}PS_{4.5}Cl_{1.5}$. For the sample milled at 500 rpm for 240 min, the splitting is not observable anymore while the center of the overall NMR line does not shift. This broadened NMR signal shows a wide distribution of inequivalent coordination environments of the PS_4^{3-} polyanions. In the ^{6}Li NMR spectra, a similar trend can be observed. The pristine sample (Figure 3c) reveals a signal that is composed of at least three different lines corresponding to different Li^{+} positions and Wyckoff 4*d* environments. In the samples milled at 500 rpm, only a single broad line is visible clearly pointing to increased disorder in the Li^{+} coordination environment. A slight shift towards higher fields may indicate small changes in the local environment of Li^{+}. High-resolution NMR data corroborate the results from the PDF analyses of increased disorder in the local structure although the exact structural disorder remains difficult to deconvolute.

Since the lithium argyrodites are polycrystalline materials, the crystallite size does not equal the size of secondary particles. Scanning electron micrographs (Figure S10a) show for the pristine sample a distribution of polydisperse particles with large particles of over 100 µm in diameter. This particle size decreases to less than 50 µm after processing in the frequency ball mill. Higher magnification reveals the presence of agglomerates, consisting of smaller particles.

For the samples processed at 500 rpm in the planetary ball mill the smallest individual particles are observed. The cumulative particle size distributions of the ultrasonicated samples (Figure S10b) confirm the large number of particles with a diameter over 50 µm in the pristine sample. After 10 min of milling at 40 Hz, a broad particle size distribution with a median particle size of 10 µm is observed. The samples processed at 500 rpm exhibit a narrower distribution with a smaller median particle size of around 5 µm. There is only a slight further decrease in particle size with longer milling time or stress number, respectively, which indicates that a minimum of particle size for these milling conditions is reached.

Discrete element simulations of milling conditions. Processing in the planetary ball mill at 500 rpm leads to a stronger reduction in crystallite and particle size as well as more disorder in the local structure compared to processing in the frequency ball mill. To better understand these observed differences between the two milling methods, simulations are performed using a discrete element method. The Hertz-Mindlin contact model[39,40] and the linear spring rolling limit model were used to determine the forces occurring when the grinding media collide. The stress energy SE and its mean value $\overline{SE}$ describe the energy transferred involved within an impact. Here we can determine the entire energy in either normal or tangential direction (shear energy) of the relative media motion, as well as the plastic energy in both directions named dissipative energy.[41] By assuming that the stressed product mass is independent of operating conditions, the stress energy is directly proportional to the stress intensity, which relates the stress energy to the stressed product mass.[42] The specific stress frequency SF_m (frequency of grinding media collisions per mass of product in mill) in the planetary ball mill (**Figure 4**a) is larger and the stress energy distribution is significantly broader when compared to the frequency ball mill. This means that more collisions occur in the planetary ball mill per product mass for a certain process time, and a broad distribution of high-energy and low-energy collisions are present. Collisions of higher energy have a high shear component, which can be explained by the rolling of the grinding media on the grinding chamber wall, while the lower dissipative stress energies mainly stem from the normal component. In contrast, the frequency ball mill (Figure 4b) predominantly shows collisions with a high normal proportion, which is because the grinding media oscillate primarily from lower wall to upper wall and back, thereby stressing above all the material between the grinding media and the grinding chamber. The higher specific stress frequency of sufficient stress energies in the planetary ball mill leads to faster comminution resulting in smaller particles. In particular, the high shear fractions and the grinding effect of the grinding media rolling on the wall ensure an additional comminution effect compared to the frequency ball mill.

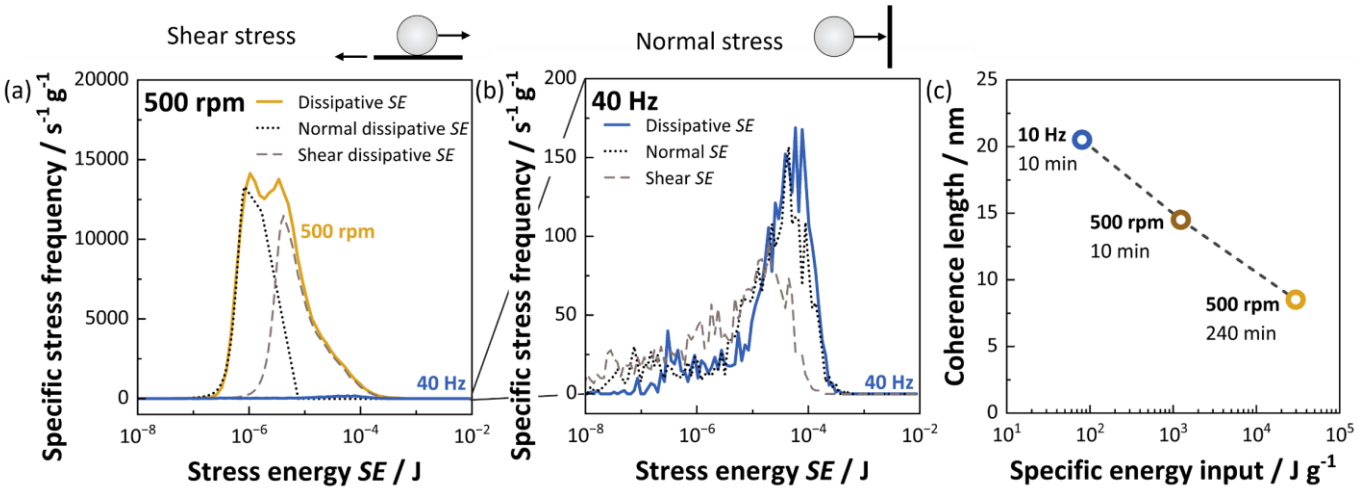


Figure 4. *(a) Specific stress frequency against dissipation stress energy curve obtained by discrete element method for the 5 mm grinding media. The dotted line represents the calculated normal component and the dashed line the shear components of the dissipative stress energy distribution. (b) Zoom-in for the frequency ball mill showing the normal components have the dominant impact in the milling process. (c) Calculated specific energy input during the different ball milling procedures correlates with the coherence lengths determined by NPDF.*

Figure 4c shows the specific energies, that act on the solid electrolyte during the milling process, for the three different milling conditions with 5 mm grinding media and compares them to the determined crystallite sizes from neutron pair distribution function analyses. For an in-depth discussion on the calculated specific energies, we refer to the Experimental Section. In short, the specific energy represents the product of the stress energy, the specific stress frequency and the time of the milling process. With increasing specific energy input, the coherence and thus the crystallinity of the solid electrolyte decreases. This can be attributed to the increasing number of stress events on the material with increasing milling time. In particular, the broad stress energy distribution present in the planetary ball mill with a high number of collisions causes a strong decrease in the crystallinity of the solid electrolyte and increased disorder in the local structure. Furthermore, the particle size exhibits a higher decrease in the planetary ball mill than in the frequency ball mill. As the reduction in particle size correlates with the total energy input, larger milling times in the frequency ball mill should further reduce the particle size. However, at a certain point the effect of caking, i.e. the aggregation of powder on the walls of the milling cup, will mitigate further comminution of (secondary) particles. To further explore the influence of the milling conditions on the stressing

and overall energy input, various parameters such as carrying the milling frequency and milling media size were simulated. These data can be found in the Supporting Information, overall showing that the stress energy increases with increasing milling speed or milling frequency (Figure S11), whereas a stronger influence of an increasing grinding media mass on the stress energy was found in the frequency mill (Figure S12).

To correlate the simulation results with additional experimental data, the argyrodite was processed with a different grinding media size of 3 mm. This results in higher specific stress frequencies with a lower stress energy in both methods during processing. The structural investigation (Figure S13) reveals similar results with only slight deviations to the samples processed with 5 mm grinding media within each set of parameters indicating that the similar specific power has a dominant influence.

Effects on ionic transport. To understand the effects of the structural changes on the ionic transport, ^{7}Li spin-lattice relaxation (SLR) NMR measurements and electrochemical impedance spectroscopy are combined to probe the local and long-range transport. The analysis of local diffusion of mobile ions by ^{7}Li SLR NMR is based on the relaxation model of Bloembergen, Purcell, and Pound (BPP).[43] Diffusion-controlled SLR rates T_1^{-1} of the mobile ions reach their maximum when the motional correlation rate reach the order of the angular Larmor frequency. The correlation rate is proportional to the ionic jump rate within a factor of 2. Analyzing the T_1^{-1} relaxation rates as a function of temperature therefore allows the determination of jump rates and activation energies of the elementary diffusion processes. The Arrhenius plots of the diffusion-induced ^{7}Li NMR T_1^{-1} relaxation rates of the pristine and processed samples are shown in **Figure 5**a. Solid lines represent the analysis according to a modified BPP model, which allows the slope of the low-temperature flank to take values lower than that on the high-T side.[44,45] From the temperature at the rate maximum T_{max}, a jump rate of 7×10^8 s^{-1} for the pristine sample can be estimated. No significant changes of T_{max} are observed between pristine $Li_{5.5}PS_{4.5}Cl_{1.5}$ and the sample processed at 40 Hz. Compared to the pristine one, the peaks referring to the samples treated in the planetary ball mill are, however, slightly shifted towards higher temperatures. These small shifts reveal that the (local) Li^+ diffusivity in the solid electrolyte has slightly decreased after processing at 500 rpm.

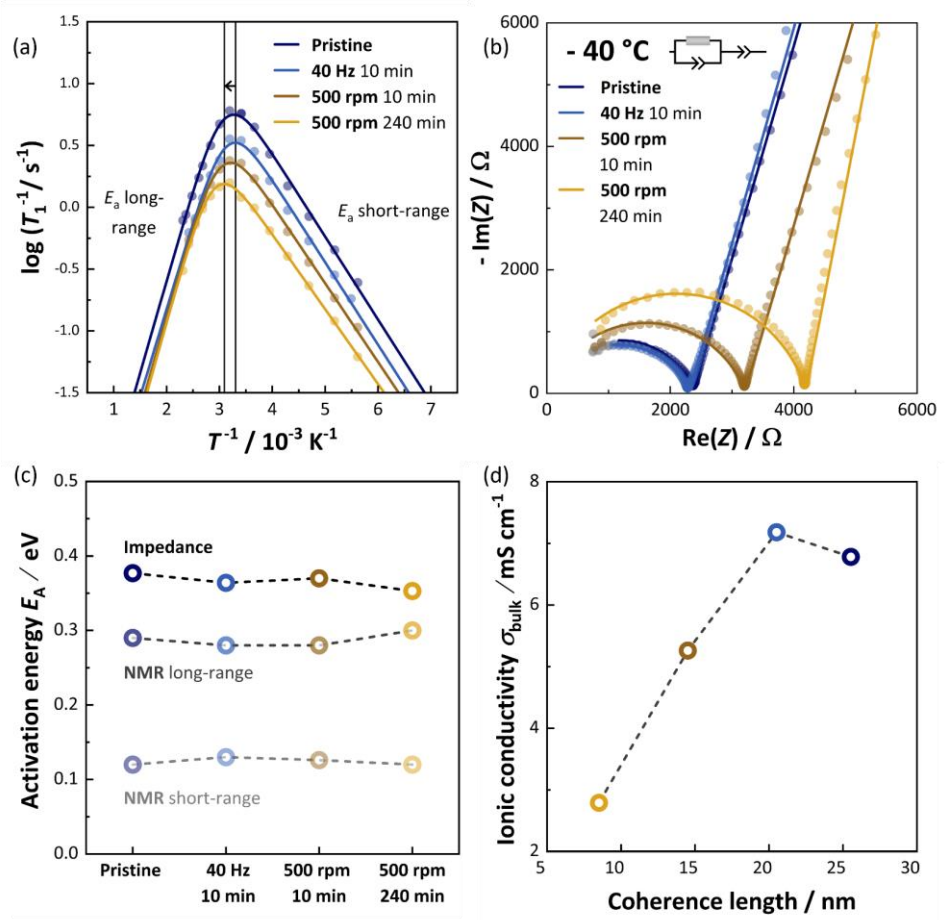


Figure 5: *(a) Diffusion-induced ^{7}Li SLR NMR rates reveal a shift of the peak maximum towards higher temperatures for the samples prepared by ball milling using planetary mills. These small shifts reveal a slightly decreased (local) Li^+ diffusivity in mechanically treated $Li_{5.5}PS_{4.5}Cl_{1.5}$. For clarity, the originally overlapping peaks were shifted down the y-axis; mechanical treatment does not significantly affect their amplitudes. (b) Nyquist plots of processed $Li_{5.5}PS_{4.5}Cl_{1.5}$ determined from impedance spectroscopy in press cells at -40 °C. (c) Comparison of activation energies determined by temperature-dependent impedance spectroscopy and ^{7}Li SLR NMR. All methods show activation energies within the uncertainty. (d) The ionic conductivity of the differently processed samples correlates with the coherence lengths obtained by NPDF.*

To further study the long-range ionic transport, temperature-dependent potentiostatic impedance spectroscopy was carried out. The impedance spectra at -40 °C can be modelled by a parallel resistor and constant phase element in series with a constant phase element (Figure 5b). No grain boundary contributions can be deconvoluted from bulk transport which is often observed for lithium argyrodites.[46] At room temperature and above only the blocking electrode contribution is detected for the pristine sample due to the high conductivity of the electrolyte (Figure S14a). The fits result in a bulk conductivity of 6.8(2) mS·cm^{-1} at room

temperature for the pristine $Li_{5.5}PS_{4.5}Cl_{1.5}$ which is in the range of previously reported values.[20] The conductivity of the sample processed in the frequency ball mill lies within the error margin. In contrast, the samples milled at 500 rpm show a major decrease in ionic conductivity with 5.3(2) $mS \cdot cm^{-1}$ after 10 min and 2.8(2) $mS \cdot cm^{-1}$ after 240 min. With the decrease in crystallinity and particle size in the longest milled sample one might expect larger contributions of grain boundary resistances, however, even at -100 °C (Figure S14b) only one semicircle is detected and bulk and grain boudary transport cannot be deconvoluted. When analysing the influence of different grinding media sizes (Figure S14c), the 3 mm grinding media exhibit slightly lower conductivities than the 5 mm grinding media within the same milling conditions. Once the necessary energy for comminution of crystallites is reached, the higher number of collisions with 3 mm grinding media might cause further reduction in ionic conductivity. However, the differences are close to the uncertainty of the measurement procedure.[47] From the temperature-dependence of the ionic conductivity the activation energies were determined via Arrhenius plots (Figure S14d). The activation energy of pristine $Li_{5.5}PS_{4.5}Cl_{1.5}$ of 0.38 eV aligns with reported literature values[20] and does not change for the processed samples. Figure 5c compares these values to the activation energies obtained from the ^{7}Li relaxometry data. The asymmetry in the fitted BPP functions allows to extract activation energies of the long-range transport from the high-temperature side of the rate peak with values between 0.28 eV and 0.30 eV which are near the values of those obtained by impedance spectroscopy. The activation energies on the low temperature flank low energy barriers for fast but localized ion diffusion in argyrodites and are in the range of 0.12 - 0.13 eV for all samples. From the combined measurements it can be concluded that all determined activation energies do not significantly change with processing. Comparing the ionic conductivities with the coherence lengths determined by neutron PDF analyses (Figure 5d) shows a clear correlation between structural coherence and ionic conductivity. With increasing ball milling energy and increasing stress number, the coherence length and ionic conductivity of $Li_{5.5}PS_{4.5}Cl_{1.5}$ both decrease. With a reduced coherence length, a decrease in the size of the crystallites is expected. The crystallites are likely to be embedded in an amorphous matrix as no grain boundary contributions could be resolved. With lower coherence, the long-range diffusion pathways might be interrupted leading to the decrease in ionic conductivity. The loss in coherence is partly reversible by annealing. When the sample processed at 500 rpm for 240 min is heated at the synthesis temperature of 450 °C for 48 h, less broadened reflections are obtained in the X-ray diffractogram (Figure S15). The coherence length extracted by XPDF is increased, but does not reach the value of the pristine sample while agglomerates of small particles are still present. The ionic conductivity increases to a value of

5.3(2) $mS \cdot cm^{-1}$ in accordance with the increased structural coherence underlining the reversibility of the milling effects.

Effects on cathode composites. Since bulk ionic conductivity and particle size trend in opposite directions for the processed samples, an analysis of the effective ionic conductivity is helpful to assess the effects of processing on the performance of cathode composites. The effective ionic conductivity σ_{eff} is determined by the bulk ionic conductivity σ_{bulk}, the volume fraction Φ_i of the conducting material in the composite and the tortuosity factor κ_i according to Equation 1.

$$\sigma_{eff} = \frac{\Phi_i}{\kappa_i} \cdot \sigma_{bulk} \qquad (1)$$

The tortuosity factor plays a crucial role in the performance of the composite.[48] Recent studies showed how smaller particle sizes of the solid electrolyte lead to lower tortuosity and higher effective ionic conductivities[21,49]. Composites of the different samples with $LiNi_{0.83}Co_{0.11}Mn_{0.06}O_2$ (NCM811) were prepared and impedance spectroscopy was measured in symmetrical cells in electron-blocking configuration to obtain the effective ionic transport (Figure S16a). The obtained impedance spectra result from convoluted contributions of ionic transport in the solid electrolyte, electronic transport in the cathode active material as well as charge transfer at the interphase of both compounds. Therefore, a T-type transmission line model (Figure S16b) was used to deconvolute the partial ionic and electronic conductivities according to Minnmann *et al.*[50]

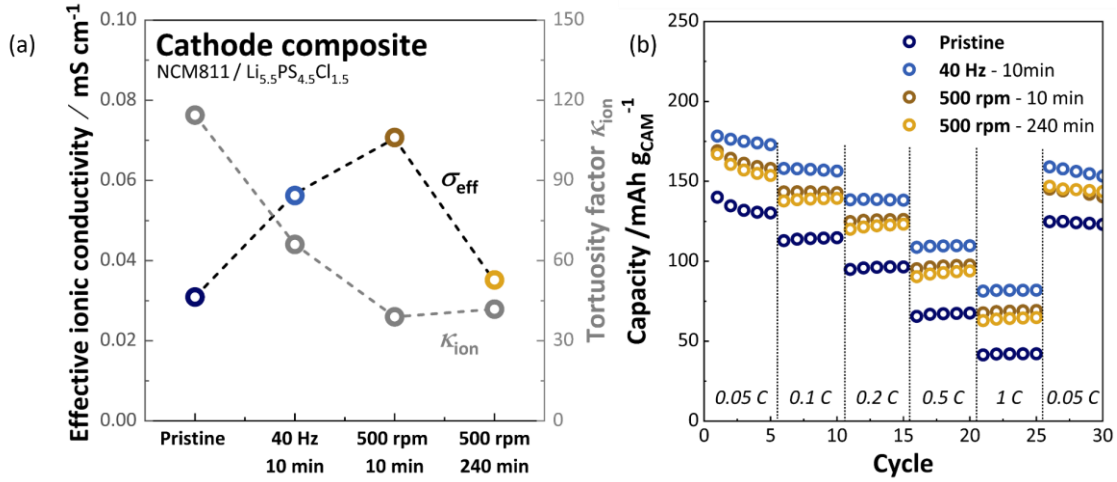


Figure 6: *(a) Measured effective ionic conductivities and calculated tortuosity factors of cathode composites of NCM811 and processed $Li_{5.5}PS_{4.5}Cl_{1.5}$. The samples that were processed at 500 rpm for ten minutes show the highest partial ionic conductivity and lowest tortuosity*

factor. (b) Rate capability tests of the four composites reveal an improved performance for shortly processed samples.

The fitted Nyquist plots are displayed in Figure S17c. The extracted effective ionic conductivities (**Figure 6**a) show a different trend to the ionic conductivities of the pure solid electrolytes. σ_{eff} increases from the pristine sample to the electrolyte processed at 40 Hz and reaches its maximum for the material that was milled at 500 rpm for 10 min. With the longer milling time of 240 min it decreases. From these effective ionic conductivities and the bulk ionic conductivities of the processed electrolytes (Figure 5d) the tortuosity factor κ_{i} of the four samples was determined. The tortuosity factor decreases with milling at 40 Hz and is the lowest after milling in the planetary ball mill where the sample milled for 10 and for 240 min exhibit nearly the same value. The lower tortuosity can also be seen in scanning electron micrographs of the composites (Figure S17). This trend is highly correlated to the measured particle size distributions which corroborates that smaller particles lead to more effective ionic transport in the composite. The re-annealed sample exhibits a better effective ionic conductivity than the pristine and the longest milled sample (Figure S18). While the particles in the annealed sample are still smaller than those of the pristine one leading to lower tortuosity, its bulk ionic conductivity is increased compared to the sample milled for 240 min.

The effect of the processed solid electrolytes on the rate-dependent cycling performance of solid-state batteries was investigated with the $Li_{5.5}PS_{4.5}Cl_{1.5}$/NCM811 cathode composites. The obtained discharge capacities at different C-rates are shown in Figure 6b. All samples exhibit a typical drop in the initial charge capacity, which is related to the loss of active lithium,[51] structural rearrangements, and contact loss.[52] The post processing that affects the microstructure and ionic partial transport affects the overall capacities, leading to higher attainable capacitites compared to using the pristine solid electrolyte. **Figure 7** schematically visualizes the two main effects that can be concluded for the processed $Li_{5.5}PS_{4.5}Cl_{1.5}$. Ball milling in the planetary ball mill leads to a continuous decrease in coherence length causing lower ionic conductivities in the pure solid electrolyte. Nevertheless, the milling decreases the particle size of the solid electrolytes. Mixed with cathode active material, the smaller electrolyte particles produce a composite with lower tortuosity factor and more effective transport pathways for Li^+ ions. For the shortly milled samples, the effect of a smaller particle size compensates the slight decrease in the bulk ionic conductivity resulting in higher effective ionic conductivity and, hence, better cell performance than the pristine sample. With a longer ball milling time of 240 minutes,

particles become only slightly smaller while the coherence length is significantly further reduced. Hence, the effective ionic conductivity and cell performance decrease.

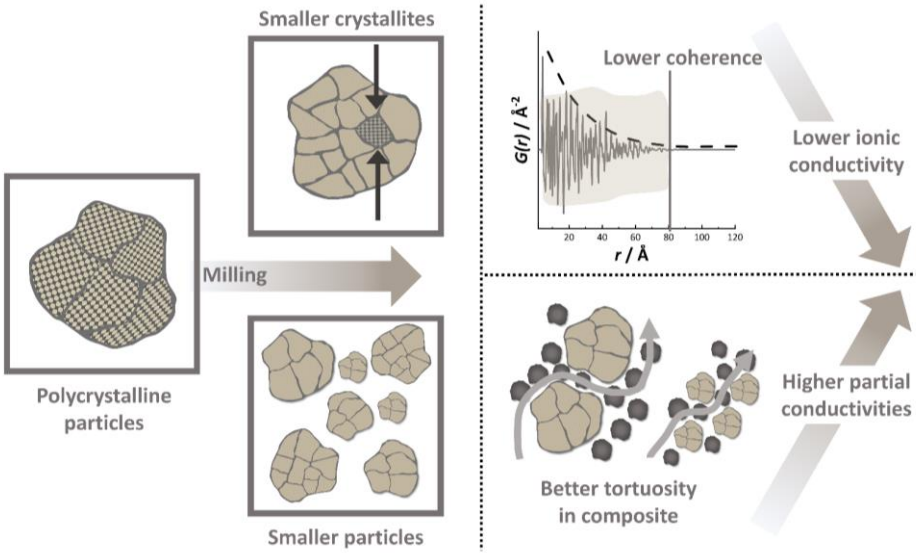


Figure 7: *Schematic representation of the two main effects of ball milling on* $Li_{5.5}PS_{4.5}Cl_{1.5}$*. While smaller crystallites reduce the ionic conductivity of the pure solid electrolyte, the decrease in particle size leads to lower tortuosity and higher effective ionic conductivities in the composite at the same time.*

3. Conclusions

Using a multitude of experimental techniques allowed the deconvolution of the various effects that post-synthesis ball milling has on the solid electrolyte $Li_{5.5}PS_{4.5}Cl_{1.5}$. A combination of XRD, NPDF and XPDF shows a decrease in structural coherence and allowed the quantification of the crystallite size and straining occurring due to the processing. PDF analyses and MAS NMR spectroscopy both observed an increase in disorder in the local structure with long ball milling times. The decrease in crystallinity correlates with lower bulk ionic conductivities for samples processed in the planetary ball mill. Furthermore, ball milling reduces the particle size of the solid electrolyte. By annealing at 450 °C these observed changes were partly reversible. The smaller particles lead to lower tortuosity factors in the cathode composites seemingly counteracting the decrease in the ionic conductivity of the solid electrolyte itself. For short ball milling times, the lower tortuosity outweighs the reduction in ionic conductivity and therefore results in a better cell performance. With longer milling times the further decreasing coherence length leads to a drop in capacity that can be achieved. Discrete element simulations shed light into the acting stresses during the ball milling process. While in the frequency ball mill collision

in normal direction have the major impact, a larger number of high energy shear stresses sum up to a much higher specific energy input in the planetary ball mill. Slightly lower ionic conductivities for smaller grinding media indicate that the decrease in crystallinity is not only affected by the energy input but also the number of collisions. This improved understanding of the milling process can be a starting point for further optimization of the milling conditions to ensure small particles while mitigating the loss of structural coherence. This work demonstrates that optimizing the post synthesis processing of solid electrolytes plays a crucial role in improving the performance of solid-state batteries, an often overlooked or rarely mentioned influence.

4. Experimental Section

Solid-state synthesis of $Li_{5.5}PS_{4.5}Cl_{1.5}$. Samples were prepared by a modified route of a previously reported synthesis.[20] The pristine electrolyte was synthesized by solid-state synthesis under inert conditions using stoichiometric amounts of Li_2S (Alfa-Aesar, 99.9%), P_2S_5 (Sigma-Aldrich, 99%) and LiCl (Alfa-Aesar, 99%). The LiCl was pre-treated in a Fritsch PULVERISETTE 7 planetary ball mill (4 hours at 500 rpm in cycles of 10 min of milling with subsequent resting time of 10 min) and all precursors were ground in a mortar for 20 minutes, pressed into pellets and filled into carbon-coated quartz ampoules which were dried at 800 °C under dynamic vacuum for two hours. The ampoules were sealed under vacuum and placed into a horizontal tube furnace at 450 °C for 48 hours after heating up with a rate of 100 °C per hour and left to cool down to room temperature. After the first annealing, the intermediate product was ground again for 20 min, pressed into pellets and heated a second time at 450 °C for 48 hours in evacuated ampoules.

Post-synthesis processing. Frequency ball mill samples were processed in a Fritsch PULVERISETTE 23 at 40 Hz for 10 min, in batches of 200 mg of pristine $Li_{5.5}PS_{4.5}Cl_{1.5}$ with 2 g of grinding media (zirconium oxide, 3 mm or 5 mm diameter). For the samples in the planetary ball mill, 1 g of pristine electrolyte was added to 10 g of grinding media (zirconium oxide, 3 mm or 5 mm) in an 80 ml zirconium oxide ball mill cup. The material was processed in a Fritsch PULVERISETTE 7 at 500 rpm for 10 min. For the long processing time, 24 cycles of 10 min ball milling at 500 rpm with subsequential pauses of 10 min were applied.

X-ray diffraction and Williamson-Hall analyses. The X-ray diffraction data were recorded using a Stoe STADI P diffractometer (Mo $K_{\alpha 1}$ radiation: λ = 0.70930 Å, Ge (111)

monochromator) in Debye-Scherrer geometry equipped with a Dectris MYTHEN2 1K detector. The samples were measured in sealed glass capillaries over a 2θ-range of 4 - 45° with a scanning rate of 1° per minute. Phase analyses and Rietveld refinements were carried out using TOPAS academics V7.[53] R_{wp}, R_{exp}, and goodness of fit (*gof*) were used as fit indicators to assess the quality of the refinement. The profile was refined by (1) a scale factor, (2) 6 free background coefficients of a Chebyshev polynomial function, (3) peak shape parameters of a modified Thompson−Cox−Hastings pseudo-Voigt function[54], (4) a full axial model to account for the asymmetry of the peak due to axial divergence as described by Cheary *et al.*[55], (5) a zero point offset, (6) the lattice parameters. With fixed profile, (7) the fractional atomic coordinates and subsequently (8) isotropic atomic displacement parameters were fit. The profile of a Nist c660 LaB_6 standard measurement was fitted by a Thompson−Cox−Hastings pseudo-Voigt function and the fixed profile was used to refine influence of strain and crystallite size in TOPAS academics V7.

Due to better peak separation and lower asymmetry, X-ray diffraction data for Williamson-Hall analyses were collected on a Stoe STADI P diffractometer with Cu $K_{\alpha 1}$ radiation (λ = 0.70930 Å) and Ge 111 monochromator in Debye-Scherrer geometry with a MYTHEN 1K detector. Sealed glass capillaries were measured in moving mode over a 2θ-range 10 - 70° with a step size of 3° and a measurement time of 360 s per step. The Williamson-Hall method was used to deconvolute the contributions of internal strain and crystallite size. The integral breadth β of the Bragg peaks was determined by fitting each Bragg peak with a pseudo-Voigt function. From the Williamson-Hall equation[35]

$$\beta \cos\theta = C\varepsilon \sin\theta + \frac{K\lambda}{d} \qquad (2)$$

with the proportionality factors C and K the contributions of internal strain ε and crystallite size d were determined.

Neutron pair distribution function (NPDF) and X-ray pair distribution function (XPDF) analyses. Neutron total scattering data were collected at 100 K and 297 K using the Nanoscale Ordered MAterials Diffractometer (NOMAD) at the Spallation Neutron Source (SNS). The samples were loaded into a 3 mm quartz capillary and then sealed in a glovebox using epoxy resin. Software available at the beamline was used to calculate the NPDF with a Q_{max} of 28 Å^{-1}. The normalized scattering intensity $I(Q)$ was produced by subtracting background signal from the event-based data followed by vanadium normalization. An arbitrary scaling factor was applied to produce structure factor $S(Q)$, so that $\lim_{Q\to\infty} S(Q) = 1$. A Fourier filter was applied to

produce the expected behavior, $\lim_{r\to 0} G(r)=-4\pi r\rho$, at the limit of the reduced pair distribution function $G(r)$.

X-ray total scattering data were recorded using a Stoe STADI P diffractometer (Ag $K_{\alpha 1}$ radiation: λ = 0.55941 Å, Ge 111 monochromator) in Debye-Scherrer geometry with four Dectris MYTHEN2 1K detectors as described by Thomae *et al.*[56] The samples were measured in sealed glass capillaries over a Q-range of 0.8-20.5 $Å^{-1}$ for 24 h. Data reduction was carried out using PDFgetX3 with a Q-range cutoff of Q_{max} = 15 $Å^{-1}$.[57]

Small box modelling of the NPDF was performed over a r range of 1.8 Å to 10 Å using PDFgui.[58] Subsequently, the (1) scale factor, (2) correlated motion factor, (3) lattice parameters, (4) atomic positions, (5) isotropic atomic displacement parameters, and (6) occupancies were refined using the cubic Rietveld refinement structure as starting model. To refine a potential rotation of PS_4^{3-} polyanions, the cubic structure obtained by small box modelling of the pristine sample was transformed into *Cm* symmetry with a $\sqrt{a}$ modulation using the ISODISTORT software[59] and the S13-S16 sulfur positions and atomic displacement parameters were refined while fixing the other structural parameters. To obtain coherence lengths, the decay of the NPDF and XPDF over a r range from 1.8 Å to 120 Å was fitted in TOPAS academics V7 with an envelope function by a spherical diameter model. The instrumental resolution parameters Q_{broad} and Q_{damp} were determined from a reference measurement of crystalline silicon.

Nuclear magnetic resonance (NMR) spectroscopy. ^{6}Li and ^{31}P magic angle spinning (MAS) spectra were recorded on a Bruker III Avance 500 NMR spectrometer connected to an ultrashielded 500 MHz magnet with a nominal field of 11.74 T resulting in resonance frequencies of 73.6 MHz for ^{6}Li and 130 MHz for ^{31}P, respectively. Chemical shifts reported refer to those of ^{6}Li in CH_3COOLi (0.1 ppm when referenced to (LiCl)) and ^{31}P in H_3PO_4 (0 ppm) measured with the help of solid $CaHPO_4$ serving as a second reference. Prior to the measurements, the polycrystalline powder samples were packed into 2.5 mm MAS rotors made of ZrO_2. The ^{6}Li and ^{31}P NMR measurements were performed at a spinning speed of 25 kHz and at 303 K (N_2 bearing gas). ^{6}Li NMR spectra were recorded with a single-pulse sequence applying a pulse length of 5.0 µs at a power level of 100 W. 32 scans were accumulated with a recycle delay of 50 s. For ^{31}P, a pulse length of 1.48 µs was applied (180 W). 64 scans were accumulated and recorded with a recycle delay of 20 s, to obtain the ^{31}P free induction decays (FIDs). Fourier transformation directly yields the NMR spectra without further manipulation of the time-domain data. For the ^{7}Li static, that is, non-MAS, NMR measurements, the samples were sealed under vacuum in Duran glass tubes (4 cm in length, 3 mm in inner diameter).

Variable-temperature spin-lattice relaxation (SLR) experiments in the laboratory frame ($1/T_1$) were performed covering a temperature range from 178 K to 413 K. The time-domain experiments were carried out with a Bruker Avance III spectrometer connected to an ultrashielded 300 MHz magnet with a nominal magnetic field of 7 T. The Larmor frequency of this field corresponds to 116 MHz for ^{7}Li. Diffusion-induced SLR rates were measured with the classical saturation recovery pulse sequence.[60] The $\pi/2$ pulse lengths, slightly depending on temperature, ranged from 2.07 to 2.75 µs if a power level of 200 W was used. To extract the rates $T_1^{-1}(1/T)$, describing the recovery of longitudinal magnetization M_z, along the z direction, the area under the corresponding FIDs was plotted against the waiting time t_d. The resulting magnetization transients $M_z(t_d)$ were analyzed with single, but stretched exponential functions $M_z(t_d) \propto 1-\exp(-t_d/T_1)^{\gamma}$ with the stretching parameter γ taking values from 0.8 and 1.0.

Scanning electron microscopy. For sample preparation, solid electrolyte powder was attached to the sample holder with double-sided carbon tape. For measurements of cathode composites, 30 mg of the prepared composite were pressed with a uniaxial pressure of 374 MPa for 3 min and the pellet was placed on the sample holder with double-sided carbon tape. The holders were coated with a layer of gold by a Cressington Sputter Coater with an applied current of 40 mA for 30 s under reduced pressure of 0.05 mbar. Scanning electron microscopy was performed at a Carl ZeissAURIGA CrossBeam working station (accelerating voltage of 3 kV) with an In-lens detector.

Particle size distribution. The particle size distribution was determined by a Sympatec Helos instrument. A small amount of the powder was placed in a small snapper with xylene and then ultrasonicated with an ultrasonic finger for approx. 15 min. The suspension was then injected into the measurement cuvette outside the glovebox for the measurement and stirred again by hand. The measurement cuvette contained a solution of 99 wt.% xylene and 1 wt.% oppanol, which was added to increase the viscosity of the solution to prevent large particles from sedimenting. Six measurements of ten seconds were recorded for each sample.

Discrete element method simulations. The simulation set-up of the frequency ball mill and the set-up of the planetary ball mill can be seen in Figure S19. For the simulation of the frequency ball mill, 2 g of grinding media were inserted, and the frequency ball mill was moved with a frequency of 40 Hz and a peak to peak amplitude of 9 mm in translational direction for 5.5 s. The properties of the grinding media (zirconia, see Table S7) were taken from the manufacturer's specifications and previous calibration tests assuming that $Li_{5.5}PS_{4.5}Cl_{1.5}$ behaves congruently with Li_6PS_5Br.[41,61] The grinding media and the grinding chamber were

calibrated as if the surface was covered with material. This enables a realistic simulation of the acting stress energies $\overline{SE}$ while reducing the simulation times. Since a stationary state was reached after about 1 s mixing time, the power data as well as the grinding media-related stress energies $\overline{SE}_{GM}$ and stress numbers *SN* between 1 s and 5.5 s were evaluated.[62] The grinding media sizes varied between 3 mm, 5 mm and 10 mm. For the simulation of the planetary ball mill, 10 g of grinding media were inserted into the simulation domain and the simulation was run for 5.5 s congruent to the simulation of the frequency ball mill. The rotational speed of the sun was set to n_{sun} = 500 rpm, which leads to a rotational speed of the grinding chamber of n_{GC} = -1000 rpm with a speed ratio of k = -2. The forces acting on the grinding media were determined by the Hertz-Mindlin contact model.[39,40] The collision powers P_i^{α} per grinding media i per output interval Δt_{out}= 0.5 ms determined from the forces were converted into collision-based mean stress energies $\overline{SE}_{GM}$ similar to Frankenberg *et al.*[62] For this purpose, the grinding media-related specific power data per time interval Δt_{out} were exported and divided by the collision frequency $\overline{c}_i$.

$$\overline{SE}_{GM}^{\alpha} = \frac{P_i^{\alpha}}{\overline{c}_i} = \frac{\sum_{k=1}^{N_{k,i}} W_k^{\alpha}}{\Delta t_{out}} \cdot \frac{\Delta t_{out}}{N_{k,i}} = \frac{\sum_{k=1}^{N_{k,i}} W_k^{\alpha}}{N_{k,i}} \quad (3)$$

$N_{k,i}$ stands for the number of collisions of grinding media i in the time interval Δt_{out}, W_k^{α} for the collision energy calculated from the contact forces, and α denotes the differentiation of the collisions into normal collision energy, tangential collision energy and dissipation collision energy. Moreover, the stress frequency was numerically determined and related to the product mass in the specific mill. Specific stress frequency - stress energy curves (SF_m – SE) of the two different processing methods were generated according to Hofer *et al.*[41] The SF_m – SE curves were used to determine the total specific number of collisions occurring per second of mixing and mass of product, which is referred to below as the specific stress frequency SF_m. By multiplying the specific stress frequency with the overall mixing time t_{mixing}, the so-called specific stress number SN_m results. The specific energy acting on the solid electrolyte or cathode material mixture, E_m, is then determined from the mean stress energy $\overline{SE}$ as well as SF_m and overall mixing time t_{mixing} or SN_m according to Equation 4.[40]

$$E_m = \overline{SE} \cdot SF_m \cdot t_{mixing} = \overline{SE} \cdot SN_m \quad (4)$$

Electrochemical analyses. All electrochemical measurements were performed in customized press cells consisting of a brass casing with PEEK insets and stain-less steel stamps of 10 mm diameter as electrodes.[63] An aluminum frame with a torque of 10 Nm applied a pressure of 50 MPa during the measurements. For potentiostatic electrochemical impedance spectroscopy measurements of pure electrolytes, the cells were filled with 250 mg of each compound and pressed with a uniaxial pressure of 374 MPa for 3 min. The measurements were controlled using the software ECLab V 13.0, while a temperature profile from -40 °C to 60 °C in 10 °C steps was applied in a *Biologic* climate chamber. Impedance spectra were recorded with a perturbation amplitude of 10 mV over a frequency range of 50 mHz to 7 MHz and analyzed with RelaxIS 3. To further investigate grain boundary contributions, the sample processed at 500 rpm for 240 min was pelletized, isostatically pressed at 413 MPa for 30 min, sputtered with a layer of gold and measured in a pouch cell with an Alpha-A impedance analyzer from Novocontrol Technologies applying an AC excitation voltage of 10.6 mV in a frequency range from 10 MHz to 50 mHz.

Preparation of cathode composites. $LiNi_{0.83}Co_{0.11}Mn_{0.06}O_2$ (MSE supplies, 140 mg, 70 weight-%) and the respective $Li_{5.5}PS_{4.5}Cl_{1.5}$ sample (60 mg, 30 weight-%) were scaled under inert conditions and mixed in a Fritsch PULVERISETTE 23 mill with 2 g of grinding media (ZrO_2, 3 mm diameter) at 15 Hz for 15 min.

Effective ionic conductivities. Determined in symmetrical cells: 100 mg of cathode composites were filled in press cells under inert conditions and pressed with a uniaxial pressure of 374 MPa for 3 min. A separator layer of pristine $Li_{5.5}PS_{4.5}Cl_{1.5}$ (80 mg) was added on each side and pressed again with a uniaxial pressure of 374 MPa for 3 min. A layer of indium foil (chemPUR, 99.99%, 100µm thickness, 9 mm diameter) and lithium foil (Li, abcr, 99.8%, 1.5 mg) were added on both sides. The cell was equilibrated at 25 °C for 6 hours under a pressure of 50 MPa and a PEIS measurement at a perturbation amplitude of 10 mV over a frequency range of 50 mHz to 7 MHz. The spectra were analyzed with RelaxIS 3 using the T-type transmission line model.[47]

Electrochemical rate performance tests. Press cells were filled with cathode composite (12 mg) and pristine $Li_{5.5}PS_{4.5}Cl_{1.5}$ (60 mg) and densified with a uniaxial pressure of 374 MPa for 3 min. Indium foil (9 mm diameter) and lithium foil (1.5 mg) were added on top of the separator. Cells were equilibrated at 25 °C for 6 hours under a pressure of 50 MPa and then cycling tests at rates

of 0.05 C (0.107 mA cm^{-2}), 0.1 C (0.214 mA cm^{-2}), 0.2 C (0.428 mA cm^{-2}), 0.5 C (1.070 mA cm^{-2}), 1 C (2.140 mA cm^{-2}) and again at 0.05 C were performed with the MACCOR for 5 charge-discharge cycles per cycling rate. Final cycling tests at a rate of 0.05 C had to be remeasured after an erroneous cycling protocol in the last rate step.

Supporting Information

The Supporting Information contains X-ray diffraction and pair distribution results, scanning electron micrographs, particle size distributions, further results from the discrete element simulations and electrochemical impedance spectroscopy data.

Acknowledgments

The research is supported by the International Graduate School for Battery Chemistry, Characterization, Analysis, Recycling and Application (BACCARA), which is funded by the Ministry for Culture and Science of North Rhine Westphalia, Germany. The authors acknowledge financial support within the cluster of competence FESTBATT funded by Bundesministerium für Bildung und Forschung (BMBF; projects 03XP0430A, 03XP0430F, 03XP0430C). We further acknowledge funding from the Deutsche Forschungsgemeinschaft under project number 459785385. HMRW thanks the FFG (Austrian Research Promotion Agency) for financial support within the project safeLIB. This research used resources at the Spallation Neutron Source, a DOE Office of Science User Facility operated by the Oak Ridge National Laboratory.

Conflict of Interest

The authors declare no conflict of interest.

Data Availability Statement

The data that support the findings of this study have been archived at https://doi.org/10.17879/06978410383.

Keywords

Solid electrolytes, processing, solid state batteries, argyrodite, mechanical milling

References

(1) Janek, J.; Zeier, W. G. A Solid Future for Battery Development. *Nature Energy* **2016**, *1* (9), 16141. https://doi.org/10.1038/nenergy.2016.141.

(2) Hatzell, K. B.; Chen, X. C.; Cobb, C. L.; Dasgupta, N. P.; Dixit, M. B.; Marbella, L. E.; McDowell, M. T.; Mukherjee, P. P.; Verma, A.; Viswanathan, V.; Westover, A. S.; Zeier, W. G. Challenges in Lithium Metal Anodes for Solid-State Batteries. *ACS Energy Lett.* **2020**, *5* (3), 922–934. https://doi.org/10.1021/acsenergylett.9b02668.

(3) Krauskopf, T.; Richter, F. H.; Zeier, W. G.; Janek, J. Physicochemical Concepts of the Lithium Metal Anode in Solid-State Batteries. *Chem. Rev.* **2020**, *120* (15), 7745–7794. https://doi.org/10.1021/acs.chemrev.0c00431.

(4) Lewis, J. A.; Cavallaro, K. A.; Liu, Y.; McDowell, M. T. The Promise of Alloy Anodes for Solid-State Batteries. *Joule* **2022**, *6*, 1418–1430.

(5) Tan, D. H. S.; Chen, Y.-T.; Yang, H.; Bao, W.; Sreenarayanan, B.; Doux, J.-M.; Li, W.; Lu, B.; Ham, S.-Y.; Sayahpour, B.; Scharf, J.; Wu, E. A.; Deysher, G.; Han, H. E.; Hah, H. J.; Jeong, H.; Lee, J. B.; Chen, Z.; Meng, Y. S. Carbon-Free High-Loading Silicon Anodes Enabled by Sulfide Solid Electrolytes. *Science* **2021**, *373* (6562), 1494–1499. https://doi.org/10.1126/science.abg7217.

(6) Janek, J.; Zeier, W. G. Challenges in Speeding up Solid-State Battery Development. *Nature Energy* **2023**, *8* (3), 230–240. https://doi.org/10.1038/s41560-023-01208-9.

(7) Murugan, R.; Thangadurai, V.; Weppner, W. Fast Lithium Ion Conduction in Garnet-Type $Li_7La_3Zr_2O_{12}$. *Angewandte Chemie International Edition* **2007**, *46* (41), 7778.

(8) Raju, M. M.; Altayran, F.; Johnson, M.; Wang, D.; Zhang, Q. Crystal Structure and Preparation of $Li_7La_3Zr_2O_{12}$ (LLZO) Solid-State Electrolyte and Doping Impacts on the Conductivity: An Overview. *Electrochem* **2021**, *2* (3), 390–414.

(9) Awaka, J.; Takashima, A.; Kataoka, K.; Kijima, N.; Idemoto, Y.; Akimoto, J. Crystal Structure of Fast Lithium-Ion-Conducting Cubic $Li_7La_3Zr_2O_{12}$. *Chemistry letters* **2011**, *40* (1), 60–62.

(10) Li, X.; Liang, J.; Chen, N.; Luo, J.; Adair, K. R.; Wang, C.; Banis, M. N.; Sham, T.-K.; Zhang, L.; Zhao, S. Water-mediated Synthesis of a Superionic Halide Solid Electrolyte. *Angewandte Chemie* **2019**, *131* (46), 16579–16584.

(11) Schlem, R.; Banik, A.; Ohno, S.; Suard, E.; Zeier, W. G. Insights into the Lithium Sub-Structure of Superionic Conductors Li_3YCl_6 and Li_3YBr_6. *Chem. Mater.* **2021**, *33* (1), 327–337.

(12) Bron, P.; Johansson, S.; Zick, K.; Schmedt auf der Günne, J.; Dehnen, S.; Roling, B. $Li_{10}SnP_2S_{12}$: An Affordable Lithium Superionic Conductor. *J. Am. Chem. Soc.* **2013**, *135* (42), 15694–15697. https://doi.org/10.1021/ja407393y.

(13) Kato, Y.; Saito, R.; Sakano, M.; Mitsui, A.; Hirayama, M.; Kanno, R. Synthesis, Structure and Lithium Ionic Conductivity of Solid Solutions of $Li_{10}(Ge_{1-x}M_x)P_2S_{12}$ (M= Si, Sn). *Journal of Power Sources* **2014**, *271*, 60–64.

(14) Zhou, L.; Minafra, N.; Zeier, W. G.; Nazar, L. F. Innovative Approaches to Li-Argyrodite Solid Electrolytes for All-Solid-State Lithium Batteries. *Accounts of Chemical Research* **2021**, *54* (12), 2717–2728. https://doi.org/10.1021/acs.accounts.0c00874.

(15) Deiseroth, H.-J.; Kong, S.-T.; Eckert, H.; Vannahme, J.; Reiner, C.; Zaiß, T.; Schlosser, M. Li6PS5X: A Class of Crystalline Li-rich Solids with an Unusually High Li^+ Mobility. *Angewandte Chemie International Edition* **2008**, *47* (4), 755–758.

(16) de Klerk, N. J. J.; Rosłoń, I.; Wagemaker, M. Diffusion Mechanism of Li Argyrodite Solid Electrolytes for Li-Ion Batteries and Prediction of Optimized Halogen Doping: The Effect of Li Vacancies, Halogens, and Halogen Disorder. *Chem. Mater.* **2016**, *28* (21), 7955–7963. https://doi.org/10.1021/acs.chemmater.6b03630.

(17) Gautam, A.; Sadowski, M.; Prinz, N.; Eickhoff, H.; Minafra, N.; Ghidiu, M.; Culver, S. P.; Albe, K.; Fässler, T. F.; Zobel, M.; Zeier, W. G. Rapid Crystallization and Kinetic Freezing of Site-Disorder in the Lithium Superionic Argyrodite Li_6PS_5Br. *Chem. Mater.* **2019**, *31* (24), 10178–10185. https://doi.org/10.1021/acs.chemmater.9b03852.

(18) Stamminger, A. R.; Ziebarth, B.; Mrovec, M.; Hammerschmidt, T.; Drautz, R. Ionic Conductivity and Its Dependence on Structural Disorder in Halogenated Argyrodites Li_6PS_5X (X = Br, Cl, I). *Chem. Mater.* **2019**, *31* (21), 8673–8678. https://doi.org/10.1021/acs.chemmater.9b02047.

(19) Hogrefe, K.; Minafra, N.; Hanghofer, I.; Banik, A.; Zeier, W. G.; Wilkening, H. M. R. Opening Diffusion Pathways through Site Disorder: The Interplay of Local Structure and Ion Dynamics in the Solid Electrolyte $Li_{6+x}P_{1-x}Ge_xS_5I$ as Probed by Neutron Diffraction

and NMR. *J. Am. Chem. Soc.* **2022**, *144* (4), 1795–1812. https://doi.org/10.1021/jacs.1c11571.

(20) Gautam, A.; Ghidiu, M.; Suard, E.; Kraft, M. A.; Zeier, W. G. On the Lithium Distribution in Halide Superionic Argyrodites by Halide Incorporation in $Li_{7-x}PS_{6-x}Cl_x$. *ACS Appl. Energy Mater.* **2021**, *4* (7), 7309–7315. https://doi.org/10.1021/acsaem.1c01417.

(21) Jiang, W.; Zhu, X.; Huang, R.; Zhao, S.; Fan, X.; Ling, M.; Liang, C.; Wang, L. Revealing the Design Principles of Ni-rich Cathodes for All-solid-state Batteries. *Advanced Energy Materials* **2022**, *12* (13), 2103473.

(22) Yanev, S.; Heubner, C.; Nikolowski, K.; Partsch, M.; Auer, H.; Michaelis, A. Editors' Choice—Alleviating the Kinetic Limitations of the Li-In Alloy Anode in All-Solid-State Batteries. *Journal of The Electrochemical Society* **2024**, *171* (2), 020512.

(23) Fu, C.; Homann, G.; Grissa, R.; Rentsch, D.; Zhao, W.; Gouveia, T.; Falgayrat, A.; Lin, R.; Fantini, S.; Battaglia, C. A Polymerized-Ionic-Liquid-Based Polymer Electrolyte with High Oxidative Stability for 4 and 5 V Class Solid-State Lithium Metal Batteries. *Advanced Energy Materials* **2022**, *12* (27), 2200412.

(24) Nagao, M.; Hayashi, A.; Tatsumisago, M. Sulfur–Carbon Composite Electrode for All-Solid-State Li/S Battery with Li_2S–P_2S_5 Solid Electrolyte. *Electrochimica Acta* **2011**, *56* (17), 6055–6059.

(25) Hakari, T.; Hayashi, A.; Tatsumisago, M. Li2S-Based Solid Solutions as Positive Electrodes with Full Utilization and Superlong Cycle Life in All-Solid-State Li/S Batteries. *Advanced Sustainable Systems* **2017**, *1* (6), 1700017.

(26) Sandoval, S. E.; Lewis, J. A.; Vishnugopi, B. S.; Nelson, D. L.; Schneider, M. M.; Cortes, F. J. Q.; Matthews, C. M.; Watt, J.; Tian, M.; Shevchenko, P.; Mukherjee, P. P.; McDowell, M. T. Structural and Electrochemical Evolution of Alloy Interfacial Layers in Anode-Free Solid-State Batteries. *Joule* **2023**, *7* (9), 2054–2073.

(27) Schweiger, L.; Hogrefe, K.; Gadermaier, B.; Rupp, J. L.; Wilkening, H. M. R. Ionic Conductivity of Nanocrystalline and Amorphous $Li_{10}GeP_2S_{12}$: The Detrimental Impact of Local Disorder on Ion Transport. *Journal of the American Chemical Society* **2022**, *144* (22), 9597–9609.

(28) Peng, L.; Yu, C.; Zhang, Z.; Xu, R.; Sun, M.; Zhang, L.; Cheng, S.; Xie, J. Tuning Solid Interfaces via Varying Electrolyte Distributions Enables High-Performance Solid-State Batteries. *Energy & Environmental Materials* **2023**, *6* (2), e12308.

(29) Wang, Y.; Hao, H.; Naik, K. G.; Vishnugopi, B. S.; Fincher, C. D.; Yan, Q.; Raj, V.; Celio, H.; Yang, G.; Fang, H.; Chiang, Y.-M.; Perras, F. A.; Jena, P.; Watt, J.; Mukherjee, P. P.; Mitlin, D. Mechanical Milling–Induced Microstructure Changes in Argyrodite LPSCl Solid-State Electrolyte Critically Affect Electrochemical Stability. *Advanced Energy Materials* **2024**, 2304530.

(30) Dewald, G. F.; Ohno, S.; Hering, J. G.; Janek, J.; Zeier, W. G. Analysis of Charge Carrier Transport Toward Optimized Cathode Composites for All-Solid-State Li− S Batteries. *Batteries & Supercaps* **2021**, *4* (1), 183–194.

(31) Banik, A.; Famprikis, T.; Ghidiu, M.; Ohno, S.; Kraft, M. A.; Zeier, W. G. On the Underestimated Influence of Synthetic Conditions in Solid Ionic Conductors. *Chemical Science* **2021**, *12* (18), 6238–6263.

(32) Wei, C.; Yu, C.; Peng, L.; Zhang, Z.; Xu, R.; Wu, Z.; Liao, C.; Zhang, W.; Zhang, L.; Cheng, S.; Xie, J. Tuning Ionic Conductivity to Enable All-Climate Solid-State Li–S Batteries with Superior Performances. *Materials Advances* **2022**, *3* (2), 1047–1054.

(33) Howell, R. C.; Proffen, T.; Conradson, S. D. Pair Distribution Function and Structure Factor of Spherical Particles. *Physical Review B* **2006**, *73* (9), 094107.

(34) Balzar, D.; Audebrand, N.; Daymond, M. R.; Fitch, A.; Hewat, A.; Langford, J. I.; Le Bail, A.; Louër, D.; Masson, O.; McCowan, C. N.; Popa, N. C.; Stephens, P. W.; Toby, B. H. Size–Strain Line-Broadening Analysis of the Ceria Round-Robin Sample. *Journal of Applied Crystallography* **2004**, *37* (6), 911–924.

(35) Williamson, G. K.; Hall, W. H. X-Ray Line Broadening from Filed Aluminium and Wolfram. *Acta metallurgica* **1953**, *1* (1), 22–31.

(36) Miranda, M. A. R.; Sasaki, J. M. The Limit of Application of the Scherrer Equation. *Acta Crystallographica Section A: Foundations and Advances* **2018**, *74* (1), 54–65.

(37) Schlenker, R.; Hansen, A.-L.; Senyshyn, A.; Zinkevich, T.; Knapp, M.; Hupfer, T.; Ehrenberg, H.; Indris, S. Structure and Diffusion Pathways in Li_6PS_5Cl Argyrodite from Neutron Diffraction, Pair-Distribution Function Analysis, and NMR. *Chemistry of Materials* **2020**, *32* (19), 8420–8430. https://doi.org/10.1021/acs.chemmater.0c02418.

(38) Wang, P.; Liu, H.; Patel, S.; Feng, X.; Chien, P.-H.; Wang, Y.; Hu, Y.-Y. Fast Ion Conduction and Its Origin in $Li_{6-x}PS_{5-x}Br_{1+x}$. *Chem. Mater.* **2020**, *32* (9), 3833–3840. https://doi.org/10.1021/acs.chemmater.9b05331.

(39) Hertz, H. Ueber Die Berührung Fester Elastischer Körper. *Journal für die reine und angewandte Mathematik* **1882**, *1882* (92), 156–171. https://doi.org/doi:10.1515/crll.1882.92.156.

(40) Mindlin, R. D. Compliance of Elastic Bodies in Contact. *J. Appl. Mech* **1949**, *16* (3), 259–268.

(41) Hofer, M.; Grube, M.; Burmeister, C. F.; Michalowski, P.; Zellmer, S.; Kwade, A. Effective Mechanochemical Synthesis of Sulfide Solid Electrolyte Li3PS4 in a High Energy Ball Mill by Process Investigation. *Advanced Powder Technology* **2023**, *34* (6), 104004.

(42) Kwade, A. A Stressing Model for the Description and Optimization of Grinding Processes. *Chemical Engineering & Technology: Industrial Chemistry-Plant Equipment-Process Engineering-Biotechnology* **2003**, *26* (2), 199–205.

(43) Bloembergen, N.; Purcell, E. M.; Pound, R. V. Relaxation Effects in Nuclear Magnetic Resonance Absorbtion. *Phys Rev* **1948**, *731679*.

(44) Jodlbauer, A.; Spychala, J.; Hogrefe, K.; Gadermaier, B.; Wilkening, H. M. R. Fast Li Ion Dynamics in Defect-Rich Nanocrystalline Li_4PS_4I─The Effect of Disorder on Activation Energies and Attempt Frequencies. *Chemistry of Materials* **2024**, *36* (3), 1648–1664. https://doi.org/10.1021/acs.chemmater.3c02988.

(45) Gombotz, M.; Hiebl, C.; Stainer, F.; Wilkening, H. M. R. Solids with Two Mobile Ions: Proton H^+ Self-Diffusion in Li–H Exchanged Garnet-Type $Li_6La_3ZrTaO_7$ as Seen by Solid-State ^1H NMR Relaxation. *The Journal of Physical Chemistry C* **2023**, *127* (23), 10960–10967. https://doi.org/10.1021/acs.jpcc.3c02330.

(46) Kraft, M. A.; Culver, S. P.; Calderon, M.; Böcher, F.; Krauskopf, T.; Senyshyn, A.; Dietrich, C.; Zevalkink, A.; Janek, J.; Zeier, W. G. Influence of Lattice Polarizability on the Ionic Conductivity in the Lithium Superionic Argyrodites Li_6PS_5X (X = Cl, Br, I). *J. Am. Chem. Soc.* **2017**, *139* (31), 10909–10918. https://doi.org/10.1021/jacs.7b06327.

(47) Ohno, S.; Bernges, T.; Buchheim, J.; Duchardt, M.; Hatz, A.-K.; Kraft, M. A.; Kwak, H.; Santhosha, A. L.; Liu, Z.; Minafra, N. How Certain Are the Reported Ionic

Conductivities of Thiophosphate-Based Solid Electrolytes? An Interlaboratory Study. *ACS Energy Letters* **2020**, *5* (3), 910–915.

(48) Bielefeld, A.; Weber, D. A.; Janek, J. Modeling Effective Ionic Conductivity and Binder Influence in Composite Cathodes for All-Solid-State Batteries. *ACS Appl. Mater. Interfaces* **2020**, *12* (11), 12821–12833. https://doi.org/10.1021/acsami.9b22788.

(49) Schlautmann, E.; Weiß, A.; Maus, O.; Ketter, L.; Rana, M.; Puls, S.; Nickel, V.; Gabbey, C.; Hartnig, C.; Bielefeld, A.; Zeier, W. G. Impact of the Solid Electrolyte Particle Size Distribution in Sulfide-Based Solid-State Battery Composites. *Advanced Energy Materials* **2023**, 2302309.

(50) Minnmann, P.; Quillman, L.; Burkhardt, S.; Richter, F. H.; Janek, J. Editors' Choice—Quantifying the Impact of Charge Transport Bottlenecks in Composite Cathodes of All-Solid-State Batteries. *Journal of The Electrochemical Society* **2021**, *168* (4), 040537.

(51) de Biasi, L.; Schwarz, B.; Brezesinski, T.; Hartmann, P.; Janek, J.; Ehrenberg, H. Chemical, Structural, and Electronic Aspects of Formation and Degradation Behavior on Different Length Scales of Ni-Rich NCM and Li-Rich HE-NCM Cathode Materials in Li-Ion Batteries. *Advanced Materials* **2019**, *31* (26), 1900985.

(52) Wang, S.; Fang, R.; Li, Y.; Liu, Y.; Xin, C.; Richter, F. H.; Nan, C.-W. Interfacial Challenges for All-Solid-State Batteries Based on Sulfide Solid Electrolytes. *Journal of Materiomics* **2021**, *7* (2), 209–218.

(53) Coelho, A. A. TOPAS and TOPAS-Academic: An Optimization Program Integrating Computer Algebra and Crystallographic Objects Written in C++. *Journal of Applied Crystallography* **2018**, *51* (1), 210–218.

(54) Thompson, P.; Cox, D. E.; Hastings, J. B. Rietveld Refinement of Debye–Scherrer Synchrotron X-Ray Data from Al2O3. *Journal of Applied Crystallography* **1987**, *20* (2), 79–83.

(55) Cheary, R. W.; Coelho, A. A. An Experimental Investigation of the Effects of Axial Divergence on Diffraction Line Profiles. *Powder Diffraction* **1998**, *13* (2), 100–106.

(56) Thomae, S. L. J.; Prinz, N.; Hartmann, T.; Teck, M.; Correll, S.; Zobel, M. Pushing Data Quality for Laboratory Pair Distribution Function Experiments. *Review of Scientific Instruments* **2019**, *90* (4), 043905. https://doi.org/10.1063/1.5093714.

(57) Juhás, P.; Davis, T.; Farrow, C. L.; Billinge, S. J. L. PDFgetX3: A Rapid and Highly Automatable Program for Processing Powder Diffraction Data into Total Scattering Pair Distribution Functions. *J. Appl. Crystallogr.* **2013**, *46*, 560–566.

(58) Farrow, C. L.; Juhas, P.; Liu, J. W.; Bryndin, D.; Božin, E. S.; Bloch, J.; Proffen, T.; Billinge, S. J. L. PDFfit2 and PDFgui: Computer Programs for Studying Nanostructure in Crystals. *Journal of Physics: Condensed Matter* **2007**, *19* (33), 335219.

(59) Campbell, B. J.; Stokes, H. T.; Tanner, D. E.; Hatch, D. M. ISODISPLACE: A Web-Based Tool for Exploring Structural Distortions. *Journal of Applied Crystallography* **2006**, *39* (4), 607–614.

(60) Epp, V.; Gün, Ö.; Deiseroth, H.-J.; Wilkening, M. Long-Range Li^+ Dynamics in the Lithium Argyrodite Li_7PSe_6 as Probed by Rotating-Frame Spin–Lattice Relaxation NMR. *Physical Chemistry Chemical Physics* **2013**, *15* (19), 7123–7132.

(61) Burmeister, C. F.; Hofer, M.; Molaiyan, P.; Michalowski, P.; Kwade, A. Characterization of Stressing Conditions in a High Energy Ball Mill by Discrete Element Simulations. *Processes* **2022**, *10* (4), 692.

(62) Frankenberg, F.; Kissel, M.; Burmeister, C. F.; Lippke, M.; Janek, J.; Kwade, A. Investigating the Production of All-Solid-State Battery Composite Cathodes by Numerical Simulation of the Stressing Conditions in a High-Intensity Mixer. *Powder Technology* **2024**, *435*, 119403.

(63) Zhang, W.; Weber, D. A.; Weigand, H.; Arlt, T.; Manke, I.; Schröder, D.; Koerver, R.; Leichtweiss, T.; Hartmann, P.; Zeier, W. G.; Janek, J. Interfacial Processes and Influence of Composite Cathode Microstructure Controlling the Performance of All-Solid-State Lithium Batteries. *ACS Applied Materials & Interfaces* **2017**, *9* (21), 17835–17845. https://doi.org/10.1021/acsami.7b01137.

For table of contents only

Post-synthesis processing affects the microstructure and crystallinity of the solid electrolyte $Li_{5.5}PS_{4.5}Cl_{1.5}$. While a reduction in particle size after short ball milling times improves the tortuosity in cathode composites, longer ball milling times decrease the coherence and the ionic

conductivity of the solid electrolyte. The specific energy input of the milling method is the decisive influence as simulations reveal.

